CSMA 2026
17ème Colloque National en Calcul des Structures
18-22 Mai 2026, Presqu'île de Giens (Var)

Finite Element Modeling of Ground-End Compression Springs Using a Morphing Hexahedral Mesh Generation Method

M. Dureuil[1], M. Paredes[1], G. Cadet[1,2]

[1] *ICA (Institut Clément Ader), Toulouse, dureuil@insa-toulouse.fr, paredes@insa-toulouse.fr*
[2] *CGR International, Sevran, guillaume.cadet@cgr-international.com*

Abstract — Because spring's ground coils exhibit strong geometric distortions, existing automatic approaches have been unable to produce consistent, high-quality hexahedral meshes. Our method morphs a structured O-grid along the evolving cross-section shape, preserving topology and nodal continuity. The resulting hexahedral meshes maintain high quality metrics and enable accurate finite element simulations that capture both global stiffness and local nonlinear effects from end-coil imperfections. This constitutes the first reliable and high-fidelity numerical reconstruction of ground-end springs.
Keywords — Digital Twin , Helical Spring , Meshing Technique

1 Introduction

Cylindrical compression springs are widely used due to their simple coiling process and high energy-storage efficiency [4]. Their stiffness and load-transfer accuracy strongly depend on the geometry of the end coils, which are commonly ground to mitigate perpendicularity defects [5, 6]. However, ground ends introduce complex geometrical features (loss of circularity, sharp edges, asymmetry, improper coil closure, non-parallelism, non-perpendicularity, and non-flatness) that significantly influence contact behavior (Figure 1) and complicate numerical modeling.

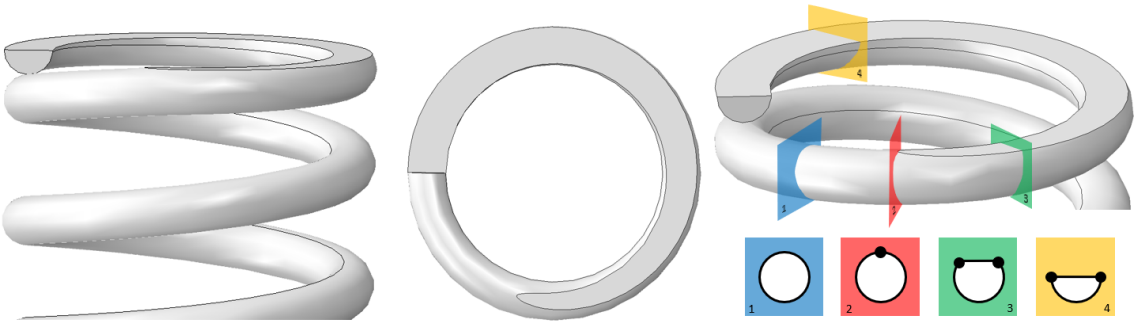

Figure 1: Front view of a ground spring (a), top view of a ground surface (b) and evolution of edges, vertices and section area of the ground end of a helical spring (c).

Existing FEM studies have largely avoided modeling the true ground geometry. Many authors either simplify the boundary conditions [9] or rely on tetrahedral elements in the end region [13, 12], despite their known limitations for spring analysis [2]. Swept or structured meshing usually fails at the transition between circular and ground cross-sections, where vertices collapse and topology changes occur (Figure 1.c). As highlighted in [2], this meshing issue is systematic in the literature but rarely acknowledged, leaving a clear gap regarding accurate, realistic FE modeling of ground-end springs.

Mesh quality metrics—aspect ratio, skewness, orthogonality, smoothness, and warping—play a key role in ensuring numerical accuracy and convergence [1, 10, 7]. Hexahedral O-grid meshes provide the best performance for springs [2], but cannot be generated directly for non-circular, evolving cross-sections. Standard strategies in Abaqus (structured, swept, or free meshing) therefore struggle to provide

a robust, fully hexahedral mesh for ground ends while maintaining a high-fidelity numerical reconstruction, motivating the exploration of more advanced solutions.

Morphing methods offer a promising alternative, as they preserve mesh connectivity while adapting to evolving geometries. Both mesh-based and meshless approaches have shown strong potential for maintaining hexahedral quality in complex geometries [11]. This makes mesh morphing particularly attractive for ground springs, where topology preservation and distortion control are critical.

The objective of this study is, therefore, to develop a dedicated morphing-based meshing methodology capable of generating high-quality, fully hexahedral finite element models of compression springs with ground ends, including realistic geometric imperfections. This approach aims to overcome the limitations of existing methods relying on tetrahedral elements or oversimplified geometries, and to provide a robust and accurate representation of manufacturing-induced deviations.

2 Method

2.1 Consideration of the defects

This study considers all major end-coil imperfections except ground-surface non-flatness, which is generally negligible but could be added in future work. The modeled defects include non-symmetric grinding planes, deviations from perpendicularity, lack of parallelism between ends, and insufficient coil closure. Four parameters are introduced for each spring end: the average grinding depth d_g, the inclination angle φ of the grinding plane, its azimuthal orientation β, and an additional end-coil pitch m_e accounting for axial offsets when it is greater than the wire diameter.

By combining these four parameters, the complete range of geometrical imperfections typically observed in ground and closed end coils can be systematically reproduced. This provides a compact yet versatile basis for simulating the influence of realistic manufacturing deviations on spring performance.

The spring geometry is described by its mean line (X,Y,Z) and local section coordinates (x,y). Global end-coil defects are converted into local parameters: the grinding depth d_g^* and deviation angle φ^*. Both are obtained from the angular studied position ω along the spring, the local grinding-plane slope p^*, and the section centroid height Z. This framework consistently derives d_g^* and φ^* from the global grinding geometry for use in the morphing procedure. All variables appear in Figure 2.

$$
\begin{aligned}
p^* &= \tan\varphi\cos(\omega-\beta) \\
\varphi^* &= \arctan(p^*) \\
d_g^* &= \frac{1}{d} max(d_g d - \frac{D\tan\varphi^*}{2} - (Z(\omega)-Z_e), 0)
\end{aligned}
$$

2.2 Morphing Strategy

The underlying assumptions of the procedure are as follows:

- A structured O-grid is used for the circular cross-sections, with 16 nodes on the circumference and 7 nodes along each diameter [2].
- The morphing process preserves mesh connectivity, maintaining the same number of nodes, edges, and hexahedral elements throughout [10].
- The strategy must accommodate geometric imperfections of the end coils.
- The resulting mesh must maximize standard quality metrics.

These assumptions inherently eliminate the issue of singular cross-sections (Figure 1.c): enforcing an O-grid topology and fixed connectivity prevents irregular node configurations and degenerate elements,

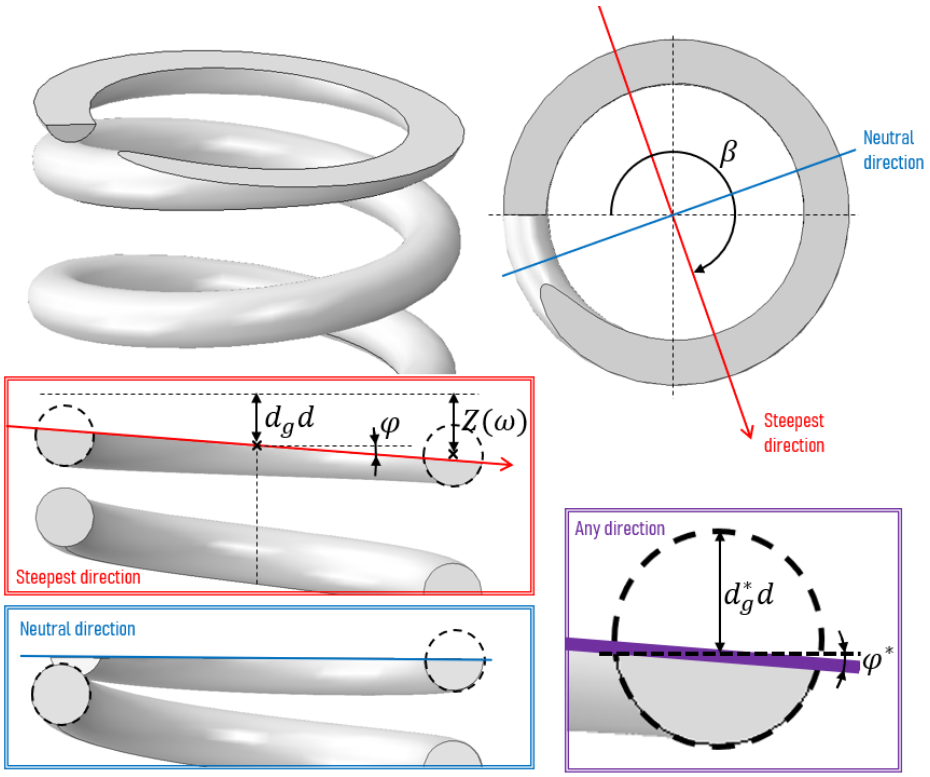

Figure 2: Graphical representation of the perpendicularity defect of the ground end coil.

thereby avoiding the severe distortions and poor FEM convergence typically associated with singular points.

However, satisfying these assumptions is challenging because the cross-section undergoes strong geometric evolution along the ground coil. As shown in Figure 3a, the main shape descriptors vary sharply with grinding depth. Even within the first 75% of material removal (corresponding to realistic grinding conditions) the area-to-squared-perimeter and height-to-width ratios decrease from 1 (circular section) to roughly 0.3 and 0.5, respectively, highlighting a rapid departure from circularity. Meanwhile, the portion of the perimeter occupied by the ground edge increases significantly, requiring a careful redistribution of circumferential nodes. In practice, nodes must progressively migrate from the circular arc toward the ground edge to preserve both geometric accuracy and mesh quality. This adaptive redistribution is central to the morphing strategy: without it, the mesh would either poorly represent the evolving geometry or suffer from unacceptable element distortion, compromising the fidelity of the CAD twin model and subsequent FEM simulations.

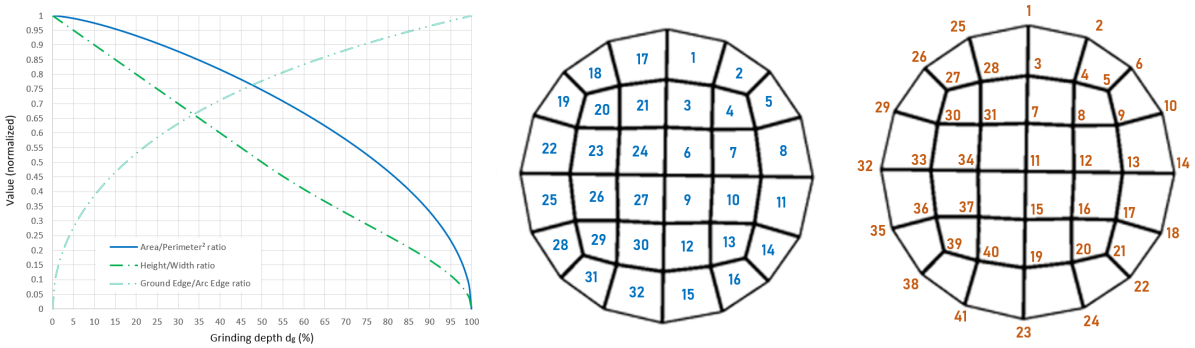

(a) (b) (c)

Figure 3: (a) Evolution of the main geometric ratios as a function of the grinding depth; (b) Face labels; (c) Node labels.

Thus, the proposed morphing procedure essentially reduces to determining the displacement of the sectional nodes as a function of the grinding depth and the prescribed geometric defects. Since the reference configuration of the unground circular section is known—namely the number of nodes, their initial positions, and their connectivity (i.e., the number and arrangement of the mesh edges) the procedure does not require any modification of the underlying mesh topology. Instead, it relies exclusively on repositioning the existing nodes in such a way that the cross-section gradually evolves from the ideal circular configuration toward the ground configuration while preserving hexahedral element consistency. This strategy ensures that the mesh remains fully structured and conformal, thereby maintaining a high degree of control over element quality while still being flexible enough to accommodate non-ideal grinding geometries.

The proposed morphing procedure for generating the spring mesh is decomposed into eight distinct steps (Figure 4). These steps are designed to ensure a systematic placement of the nodes along each section while minimizing the number of required parameters. At the same time, they guaranty the robustness of the procedure by preventing critical meshing errors, such as overlapping nodes, non-manifold faces, or inconsistencies in connectivity. Furthermore, the methodology is tailored to preserve mesh regularity and maximize element quality, which is essential to obtain reliable FEM results.

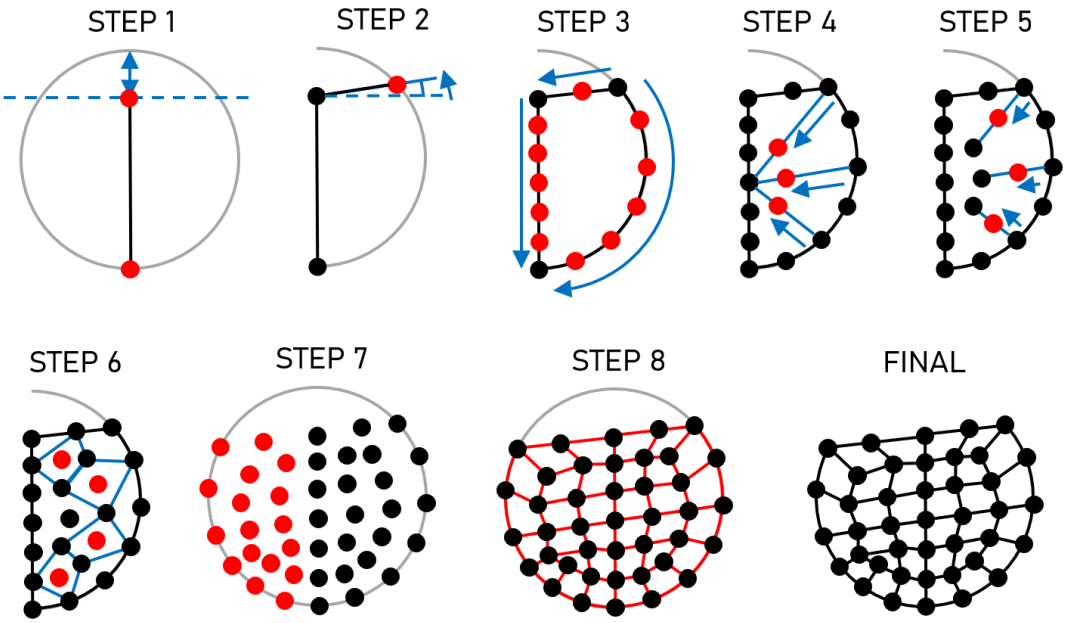

Figure 4: Graphical explanation of the mesh morphing procedure, step by step.

STEP 1 Nodes 1 and 23 are fixed on the section's mid-axis, with Node 23 at the bottom and Node 1 at the local median grinding depth d_g^*. This anchoring provides a stable reference for positioning other nodes. Local coordinates (x, y) are defined relative to the wire centroid, ensuring consistent referencing to the undeformed geometry and facilitating morphing transformations.

$$x_1 = 0 \quad , \qquad y_1 = \frac{d}{2} - d_g^* d$$

$$x_{23} = 0 \quad , \qquad y_{23} = -\frac{d}{2}$$

STEP 2 The node at the end of the ground surface is positioned according to the local grinding depth d_g^* and perpendicularity defect φ^*. Its assignment depends on d_g^*, as deeper grinding requires more elements along the flat surface. This adaptive placement preserves geometric fidelity and ensures a balanced element distribution around the section.

$$x_i = \frac{-2p^* y_1 + \sqrt{(1+p^{*2})d^2 - 4y_1^2}}{2(1+p^{*2})}, \qquad y_i = c_1 x + y_1 \qquad i = \begin{cases} 2, & \text{if } d_g^* < 0.11, \\ 6, & \text{if } 0.11 \le d_g^* < 0.3, \\ 10, & \text{if } 0.3 \le d_g^* \end{cases}$$

STEP 3 Nodes along the half-section perimeter and central axis are normally equidistributed, but two biases are introduced to smooth transitions onto the ground surface and reduce element distortion. One bias moves the node approaching the ground extremity closer to its target, while the other repositions the node leaving the extremity toward its successor, ensuring gradual redistribution and improved element regularity.

STEP 4 The O-grid structure for a circular section divides the half-section into four quadrants, guiding node placement. Along the diagonals, nodes 8, 12, and 16 are positioned using a weighted average biased toward the central node (node 11), ensuring alignment with the O-grid and minimizing distortion in non-circular regions.

$$\begin{bmatrix} x_k \\ y_k \end{bmatrix} = \frac{1}{1+W_m}\left(\begin{bmatrix} x_i \\ y_i \end{bmatrix} + W_m \begin{bmatrix} x_j \\ y_j \end{bmatrix}\right), \qquad (i,j,k) \in \mathcal{S}_m,$$

$$\begin{aligned} W_1 &= 0.6, \quad \mathcal{S}_1 = \{(11,6,8),(11,26,31)\}, \\ W_2 &= 0.8, \quad \mathcal{S}_2 = \{(6,8,5),(26,31,27)\}, \\ W_3 &= 0.4, \quad \mathcal{S}_3 = \{(11,14,12),(11,32,34)\} \end{aligned}$$

STEP 5 The next set of nodes (5, 13, and 21) is placed along the diagonals between the outer boundary and the previously positioned nodes. This hierarchical approach ensures consistent placement, prevents overlaps, and preserves the O-grid connectivity even when the section geometry deviates from circular symmetry due to grinding.

$$\begin{aligned} W_4 &= 0.8, \quad \mathcal{S}_4 = \{(14,12,13),(32,34,33)\}, \\ W_5 &= 0.7, \quad \mathcal{S}_5 = \{(11,22,16),(11,38,37)\}, \\ W_6 &= 1.0, \quad \mathcal{S}_6 = \{(22,16,21),(38,37,40)\}. \end{aligned}$$

STEP 6 The last nodes of the half-section are placed at the barycenters of quadrilaterals formed by previously positioned nodes. This ensures systematic placement in empty spaces, avoids overlaps, maintains uniform distribution, and preserves element connectivity while adapting to the geometry changes caused by grinding.

$$\begin{bmatrix} x_k \\ y_k \end{bmatrix} = \frac{1}{4}\left(\begin{bmatrix} x_i \\ y_i \end{bmatrix} + \begin{bmatrix} x_j \\ y_j \end{bmatrix} + \begin{bmatrix} x_\ell \\ y_\ell \end{bmatrix} + \begin{bmatrix} x_m \\ y_m \end{bmatrix}\right),$$

$$(i,j,\ell,m,k) \in \{(2,5,3,8,4),\ (5,8,10,13,9),\ (13,16,18,21,17),\ (16,21,19,24,20)\}$$

STEP 7 By analogy, the second half-section can be generated by repeating STEPS 2 through 6, but with an opposite grinding slope relative to that of the first half-section. A simple geometrical symmetry cannot be applied in this case, except in the trivial situation where the ground surface is free from any geometric defects.

$$x_i = \frac{-2p^* y_1 - \sqrt{(1+p^{*2})d^2 - 4y_1^2}}{2(1+p^{*2})}, \qquad y_i = c_1 x + y_1 \qquad i = \begin{cases} 25, & \text{if } d_g^* < 0.11, \\ 26, & \text{if } 0.11 \le d_g^* < 0.3, \\ 29, & \text{if } 0.3 \le d_g^* \end{cases}$$

STEP 8 Finally, all nodes of the cross-section are positioned, completing the discretization of a single section. Each subsequent section of the spring is then generated by applying the same sequence of steps, ensuring methodological consistency throughout the geometry. Once all sections are defined, the nodes can be systematically connected by edges and faces, thereby forming the hexahedral mesh cells of the final spring model.

This structured procedure not only guarantees mesh coherence across the entire component but also provides a robust framework for capturing both ideal geometries and the geometric imperfections induced by grinding. The proposed meshing structure is shown in Figure 5.

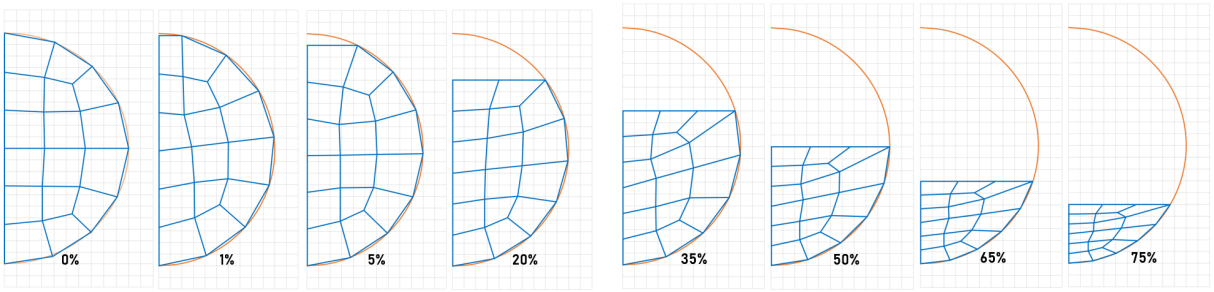

Figure 5: Proposed mesh structure in function of the grinding depth.

3 Experimental and Numerical data

The two springs analyzed in this study have already been investigated in previous scientific works [8, 5]. Both exhibit significant grinding defects at their end coils and can be useful to test our method. The main geometric properties of each spring are summarized in Table 1. Each end coil was also individually analyzed to quantify its geometric features. Among these, the end coil factor f — a geometric descriptor already introduced in the literature [3] — characterizes the winding pitch configuration of the end coil prior to grinding. Both springs were experimentally tested under axial compression using a standard parallel-plate testing setup. The material is a 17-7 PH stainless steel. Its mechanical properties were retrieved using accurate analytical models capable of predicting the stiffness of ground-end helical springs [5]. The material parameters are as follows: Young's modulus $E = 203\,400$ MPa, Poisson's ratio $\nu = 0.341$, and shear modulus $G = 75\,840$ MPa. It is worth noting that the free lengths L_0 reported correspond to measurements taken along the central axis of the spring. Consequently, due to the presence of geometric defects, these values may be slightly smaller than the actual physical free lengths.

Table 1: Geometric parameters of both tested springs

Geometric measurements		Spring 1	Spring 2
Wire Diameter (mm)	d	1.8	1.8
External Diameter (mm)	D_e	30.6	16.2
Number of Active Coils	n_a	2	10
Free Length (mm)	L_0	21.88	50.24
Top closing pitch (mm)	m_e	1.8	1.8
Top grinding depth (%)	d_g	39	60
Top end coil factor	f	0.4	0.5
Top grinding defect angle (deg)	φ	0	0
Top grinding defect orientation (deg)	β	0	0
Bottom closing pitch (mm)	m_e	2	1.95
Bottom grinding depth (%)	d_g	40	35
Bottom end coil factor	f	0.65	0.75
Bottom grinding defect angle (deg)	φ	1.39	3.18
Bottom grinding defect orientation (deg)	β	-50	310

The FE models of the two springs presented were generated using the morphing-based meshing method introduced previously, parameterized with experimentally measured geometric values (all 4 springs are shown in Figure 6). The resulting model is, therefore, an orphan meshed volume, meaning that no underlying CAD geometry is associated with the mesh. Consequently, since contact interactions are typically defined based on the surfaces of the original geometry (which are absent in this case), specific node sets were automatically defined. The nodes belonging to the upper and lower surfaces of all spring coils were concatenated into two distinct node sets, between which a surface-to-surface hard contact interaction was established, with a friction coefficient of 0.3. Two rigid compression planes were also introduced to reproduce the parallel compression supports used in experimental setups. However, due to the presence of significant geometric defects, the spring in its free state is not necessarily perfectly

aligned or perpendicular to the compression planes. This misalignment could lead to spurious deviations in the resulting force–displacement response. To ensure proper contact between the ground planes and the ground surfaces of the spring, and thus to obtain an accurate representation of the spring stiffness behavior, the simulation procedure was divided into three sequential steps.

The FE models of the two springs were created using the morphing-based meshing method with experimentally measured geometries, resulting in orphan meshes without underlying CAD (all 4 springs are shown in Figure 6). Node sets were defined on the upper and lower coil surfaces to establish hard contact with a friction coefficient of 0.3. Rigid compression planes replicated experimental supports. Due to geometric defects, the free spring may be misaligned, so reaction forces are recorded during unloading to ensure proper contact and accurately capture the spring's stiffness response (consistent with the conventional experimental procedure).

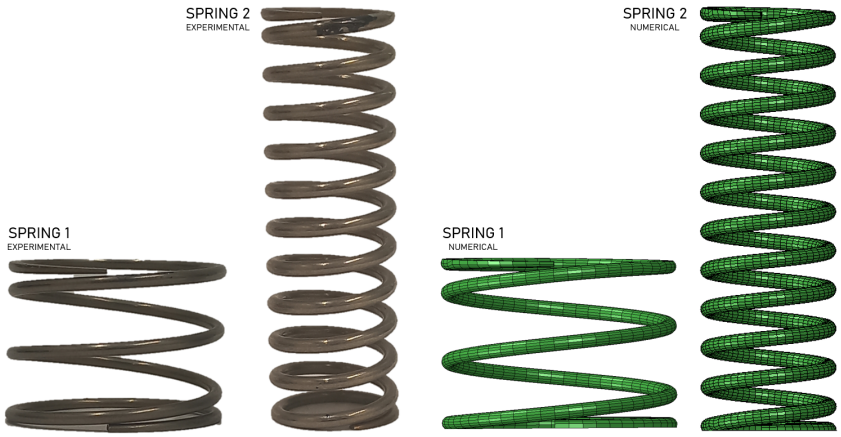

Figure 6: Experimentally and numerically tested springs.

4 Results and Discussion

A preliminary mesh quality assessment in Abaqus/CAE focused on the end coils of both springs, analyzing element aspect ratios. Only a small fraction (4.6%) of elements in these coils exceeded twice the mean aspect ratio, indicating a largely uniform, well-shaped, fully hexahedral mesh with minimal distortion. Elements maintained near-ideal square faces, good skewness, orthogonality, and parallelism, with no singularities along the ground surfaces. Localized biasing further limited warping to only a few cross-sections.

Load–displacement comparisons with experiments show that the digital twins accurately predict both global stiffness and the initial nonlinearity caused by end-coil perpendicularity defects, confirming the robustness and reliability of the morphing-based meshing strategy for ground-ended compression springs.

5 Conclusion

This work addresses the long-standing challenge of generating fully hexahedral meshes for ground-end compression springs, whose complex and evolving geometries, caused by grinding, prevent traditional meshing methods from maintaining topology and element quality. The proposed morphing-based strategy is the first to produce 100% hexahedral meshes for such springs while preserving geometric fidelity and controlling element distortion. By enforcing consistent nodal distribution and mesh connectivity, it prevents singularities and ensures smooth transitions along the ground surfaces, achieving a balance between numerical robustness and physical accuracy. The method also faithfully represents manufacturing imperfections, enabling reliable prediction of stress, contact behavior, and stiffness. Validation against experimental load–displacement curves confirms its accuracy in reproducing both global stiffness and initial nonlinear response. Future developments may include quadratic elements and direct integration with 3D scans for automated defect-based modeling.

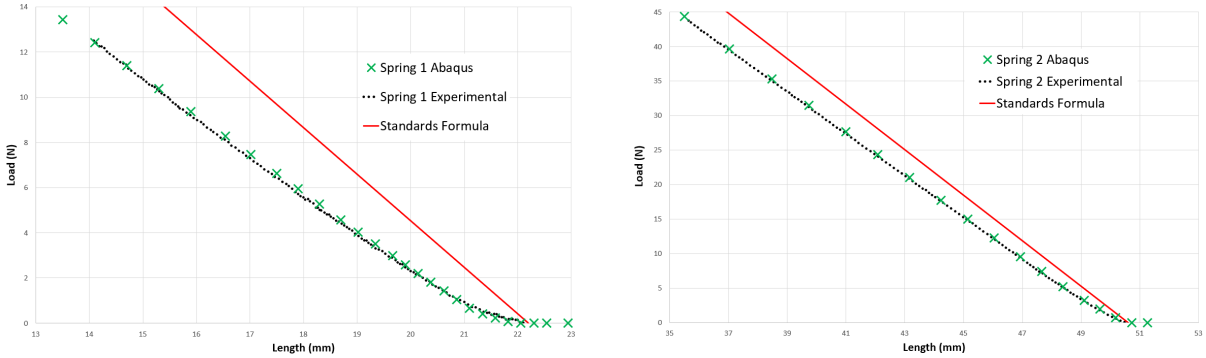

(a) (b)

Figure 7: Load-Length curves of both springs 1 (a) and 2 (b). Comparison of the experimental data with the numerical results.

References

[1] *ABAQUS/Standard User's Manual, Version 6.9*, Dassault Système Simulia Corp, 2009.

[2] G. Cadet, M. Paredes, *Convergence analysis and mesh optimization of finite element analysis related to helical springs*, Mechanics and Industry, 2024.

[3] G. Cadet, M. Paredes, H. Orcière, *Improved analytical model for cylindrical compression springs not ground considering end behavior of end coils*, Mechanics and Industry, 2021.

[4] G. Cadet, M. Paredes,*Mechanical springs: from historical origins to modern applications*, HAL Archive, 2024.

[5] G. Cadet, M. Paredes, H. Orciere, *Modèle analytique amélioré pour les ressorts de compression cylindriques meulés en prenant en compte le défaut de parallélisme de leurs surfaces d'appui*, 18ème Colloque national S.mart, 2023.

[6] EN-15800, *Cylindrical helical springs made of round wire - Quality specifications for cold coiled compression springs*, AFNOR, 1993.

[7] P.M. Knupp, *Remarks on mesh quality*, 45th AIAA Aerospace Sciences Meeting and Exhibit, 2007.

[8] M. Paredes, *Enhanced Formulae for Determining Both Free Length and Rate of Cylindrical Compression Springs*, Journal of Mechanical Design, 2016.

[9] P. Pratim, S. Balodi,*Experimental Characterisation and FEA Comparison between Wave and Helical Springs*, Proceedings of the Institution of Mechanical Engineers, Part C: Journal of Mechanical Engineering Science, 2022.

[10] T. Sorgente, S. Biasotti, G. Manzini, M. Spagnuolo, *A Survey of Indicators for Mesh Quality Assessment*, Computer Graphics Forum, 2023.

[11] M.L. Staten, S.J. Owen, S.M. Shontz, A.G. Salinger, T.S. Coffey, *A Comparison of Mesh Morphing Methods for 3D Shape Optimization*, Quadros, W.R. (eds) Proceedings of the 20th International Meshing Roundtable. Springer, Berlin, Heidelberg, 2011.

[12] H. Zhang, G. Tao, Z. Wen, *Simulation analysis of effect of wheel out-of-roundness on dynamic stress of coil springs in metro vehicles*, Engineering Failure Analysis, 2023.

[13] C. Zhou, M. Chi, Z. Wen, X. Wu, W. Cai, L. Dai, H. Zhang, W. Qiu, X. He, M. Li, *An investigation of abnormal vibration – induced coil spring failure in metro vehicles*, Engineering Failure Analysis, 2020.